ANALYZING FLOOD-INUNDATION PATTERNS USING LANDSAT DATA: A CASE STUDY OF THE MISSION RIVER FLOODPLAIN, TEXAS

A Thesis

by

DONGSHUO LU

Submitted to the Office of Graduate and Professional Studies of
Texas A&M University
in partial fulfillment of the requirements for the degree of

MASTER OF SCIENCE

Chair of Committee,	Anthony M. Filippi
Co-Chair of Committee,	İnci Güneralp
Committee Members,	Burak Güneralp
	Rusty Feagin
Head of Department,	David Cairns

May 2020

Major Subject: Geography

ABSTRACT

Flood inundation is widely acknowledged as a significant factor in the healthy functioning of floodplains. However, increasing human activities, particularly over the past several decades, have threatened the original river systems. Analyzing inundation patterns of floodplains can provide insights into the planning for unregulated floodplains, or restoration strategies for destroyed floodplain ecosystems. A case study was conducted to examine the inundation patterns of the Mission River Floodplain (MRF) in both the spatial and temporal dimensions. In this study, we proposed a weighted approach to derive the flood inundation frequency and examined its relationship to the coastal ecosystems. Exceedance probabilities of the Mission River were calculated based on daily flow from water year 1939 to 2018. Then, flood-inundation information was extracted from 135 multitemporal Landsat satellite images acquired between 1984 and 2018 to create an inundation frequency map, with weights derived from the exceedance probabilities. The inundation frequency map was jointly analyzed with several factors to determine the spatial patterns of inundation. Results reveal a strong relationship between inundation frequency and land cover, as well as soil types. Inundation frequency exhibited a stronger relationship with elevation than slope. To examine the temporal patterns of inundation, a multiple linear regression model for inundation percentage was generated. Result reveals a strong relationship between inundation percentage and discharge or precipitation. Long-term inundation dynamics were determined based on historical discharge and precipitation records. Understanding the spatial and temporal patterns of flood inundation is essential

for effective ecological restoration and management of coastal riverine ecosystems, and thus, for achieving their sustainability in the presence of the changing nature of flood events.

ACKNOWLEDGEMENTS

First and foremost, I would like to give my sincere gratitude to my committee chair, Dr. Anthony M. Filippi, my committee co-chair Dr. İnci Güneralp, and my committee members, Dr. Burak Güneralp, and Dr. Rusty Feagin, for their consistent guidance and extraordinary patience throughout this research. They walked me through all the stages of this research and the writing of this thesis.

I also appreciate all my friends and classmates for their invaluable advice and assistance with my research. It has been their suggestions that have made many things clearer. Thanks also to their care for me and company, which has made my life at Texas A&M University more fulfilling.

Last but not least, thanks to my beloved mother and father for their encouragement and great confidence in me all through these years. Thanks also to my girlfriend for her love and company.

CONTRIBUTORS AND FUNDING SOURCES

Contributors

This work was supervised by a thesis committee consisting of Dr. Anthony M. Filippi, Dr. İnci Güneralp, and Dr. Burak Güneralp of the Department of Geography, and Dr. Rusty Feagin of the Department of Ecosystem Science and Management.

The automatic water extraction in section 3.1 was completed with the help of PhD student Cesar Ricardo Castillo. The analysis of hydrological data in section 3.2 was completed in part by Dr. İnci Güneralp. Dr. Rusty Feagin was consulted on the modified land-cover classification system used in section 5.2.

Funding Sources

There are no outside funding contributions to acknowledge related to the research and compilation of this document.

TABLE OF CONTENTS

Page

LIST OF FIGURES

Page

LIST OF TABLES

Page

1. INTRODUCTION

Floodplains are flat areas adjacent to rivers or streams that flood during periods of high discharge. Floods could leads to significant and negative social-economic impacts at a global scale (Wu et al., 2014). Hoverer, not all floods are associated with natural disasters. Floodplain flow is essential for the healthy functioning of river systems, which affects water balance and floodplain ecologies (Alsdorf et al., 2007; Chormanski et al., 2011). Regular floods contribute to the lateral interaction of organic matter and nutrients between water and land, resulting in the high productivity of floodplain ecosystem (Junk, Bayley, & Richard, 1989; Tockner, Malard, & Ward, 2000). Floods can disperse seeds, deposit nutriments around roots of plants in the floodplain, and enable aquatic creatures to colonize different habitats (Huang, Chen and Wu et al 2014), thus contribute to the prosperity of flora and fauna communities.

In the past decades, intervene of human has already accelerated or decelerated natural processes, altered and destroyed floodplain ecosystems (Callan & Friedl, 2008; Syvitski et al., 2012, Gibbs et al., 2016). To maintain the floodplain ecological diversity and restore damaged aquatic habitats, it is important to identify the natural inundation dynamics of rivers and their associations with floodplain communities (Benke et al., 2000; Robertson et al., 2001; Overton, 2005). Inundation dynamics refer to the spatial and temporal pattern of inundation events. The temporal pattern includes the timing, frequency, and duration of inundation throughout the floodplain. The spatial pattern describes the area that is likely to be inundated (Benke et al., 2000). Determining inundation patterns among different river-floodplain ecosystems requires long-term

observations. Monitoring the inundation dynamics allows for better understanding of the structural and functional aspects of river-floodplain ecosystems (Benke et al., 2000).

In situ measurement is crucial to understand inundation dynamics of surface water, and has the advantage of high accuracy. However, it is hard to obtain a synoptic view of rivers especially in sparsely gauged regions. In situ measurements for river discharge provide only one-dimensional observations of inundation and storage, which cannot been applied in complex floodplains or wetland to measure the three-dimensional process varying in both space and time (Alsdorf et al., 2007). Furthermore, the difficulty of establishing spatial relationships between the main channel and connected floodplains greatly constrains the applicability of in situ measurements (Huang et al., 2014). It is also expensive and time-consuming to monitor long-term wetland dynamics using in situ measurement (Halabisky et al., 2016).

Remote sensing has become an effective and efficient tool in ground water observations (Ji et al., 2009; Chen et al., 2013; Huang et al., 2014; Lettenmaier et al., 2015). Remote sensing enables both fine-scale and large-scale water bodies mapping with spatial continuity, and provides long-term continuous monitoring of variations that are impossible or expensive to conduct with in situ measurement (Overton, 2005; Alsdorf et al., 2007; Lettenmaier et al., 2015). Time-series remote sensing provides insights into the dynamics of surface water changes, from which we can better understand the hydrology and ecology of wetland systems (Ward et al., 2014). An integration of remote sensing data and in situ measurements can lead to better insights of floodplain inundation dynamics,

flood monitoring and other hydrological applications (Ordoyne & Friedl, 2008; Huang et al., 2014).

Inundation extent and inundation frequency are the two broad categories that most previous studies have measured (Ordoyne & Friedl, 2008; Gibbs et al., 2016). Inundation extent varies with the topography, tide, human alteration and duration of the flood wave (Syvitski et al., 2012), which is closely related to the prosperity of flora and fauna communities in river-floodplain systems (Chormanski et al., 2011; Zhao et al., 2011; Huang et al., 2014). Monitoring the long-term variations in inundation extent allows for detecting fluctuations concealed from investigation based on only one or few satellite images (Song, et al 2018). Several studies (Gibbs et al., 2017; Song et al., 2018) have used remotely sensed data to map the wetland inundation dynamics at global or local scale. However, they failed to link the inundation dynamics with the ecological factors such as vegetation and wetland types, which is crucial to analyze the ecological impacts of inundation dynamics (Chen et al., 2014; Jin et al., 2017). Some others (Chormanski et al., 2011; Chen et al., 2014; Ward et al., 2014; Tulbure et al., 2016; Jin et al., 2017) related inundation dynamics with factors including vegetation types and distribution, wetland types, tide and precipitation. They examined the association between the advance or retreat of surface water and the distribution or condition of vegetation, but failed to consider the influence of different inundation frequency.

Inundation frequency is a significant characteristic of floodplain inundation (Huang et al., 2014). Primary production within floodplains is associated with changes to flood frequency (Robertson et al., 2001). Measuring inundation frequency in the past

allows for determining environmental water requirements of the floodplain-river system (Huang et al., 2012). Several previous studies (Ward et al., 2014; Tulbure et al., 2016; Song et al., 2018) have applied time-series remote sensing data to generate inundation frequency maps at local scale. Their products provided valuable information for understanding long-term inundation dynamics, but none of them considered the impacts caused by temporal bias of observations when creating inundation frequency maps.

Temporal bias means when creating inundation frequency maps, factors including revisit period of the satellite, cloud cover and the observation length (Overton, 2005; Chormanski et al., 2011) are not considered, and thus, the results could be temporal biased and may not be able to accurately represent the inundation frequency of a longer period. Landsat data is among the most widely-used optical sensors for water resources observations (Feyisa et al., 2014). However, Landsat cannot capture all ephemeral flood events including the peaks and retrieves due to the 16-day revisit time (Overton, 2005; Hui et al., 2008; Tulbure et al., 2016). Song et al. (2018) noted that the number of cloud-free images in wet seasons is typically less than that in dry seasons. If remotely sensed data cover a relatively dry period, it will lead to the underestimation of the inundation frequency and the simulated future inundation probability, and vice versa (Huang et al., 2014). Other studies have also stressed the importance of accounting for seasonality across dry and wet years (Ji et al., 2009; Tulbure et al., 2016). Song et al. (2018) assigned different weights to the images acquired in dry and wet seasons. However, the derived water frequency maps could be biased in their study.

This study is designed to examine the both the spatial and temporal patterns of floodplain inundation by creating an inundation frequency map and deriving long-term inundation dynamics. The main objectives of this study are to:

(1) Examine the long-term inundation dynamics of the Mission River Floodplain (MRF), integrating Landsat satellite data, river discharge and precipitation.

(2) Analyze the relationship between inundation frequency and land-cover types, soil types, elevation and slope.

2. STUDY AREA AND DATA

2.1 Study Area

Mission River is a lowland meandering river flowing through the coastal plains of Texas to its mouth on Mission Bay (Fig. 1). It flows on undulating coastal prairies covered by loam, clay, and sand. The floodplain provides habitats for a variety of species of waterfowl, mammals and aquatic creatures. Mean monthly temperature ranges from 15.6°C in January to 27.7 °C in August. Mean annual precipitation is 1016 mm within the floodplain, with a mean monthly precipitation ranging from 38 mm in March to 177 mm in September (https://www.usclimatedata.com/climate/refugio/texas/united-states/ustx1129). In the study area, there is a United States Geological Survey (USGS) gauge station (USGS 08189500). Mean river discharge is 2.0 m^3/s based on the records from the gauge station. The low-relief floodplain is susceptible to floods induced by meteorological and hydrological events. The river discharge increases dramatically when flood events occur. The largest flood event during the study period was in September 2001, with a peak discharge of 786.55 m^3/s.

The study area for inundation analysis was the coastal region of the Mission River Floodplain (MRF), located between 28°15'24.9"N 97°18'42.4"W and 28°09'41.2"N 97°09'44.0"W (Fig. 1). The determination of the study boundary was based on the 100-year-flood boundary for Refugio Country, Texas, which was obtained from the Flood Insurance Study supported by Federal Emergency Management Agency (FEMA; https://msc.fema.gov/portal/search). To examine the influence of tree-canopy cover of the

study area, we downloaded the Land Cover Database (NLCD) 2011 Percentage Tree Canopy – Cartographic (USDA Forest Service Remote Sensing Applications Center & U.S. Geological Survey, 2015). Because optical sensors have limited ability of penetrating tree canopy to detect the water bodies (Di Vittorio & Georgakakos., 2017), we excluded the upstream area of Mission River within the FEMA 100-year-flood boundary, where the mean canopy-cover percentage was above 50%.

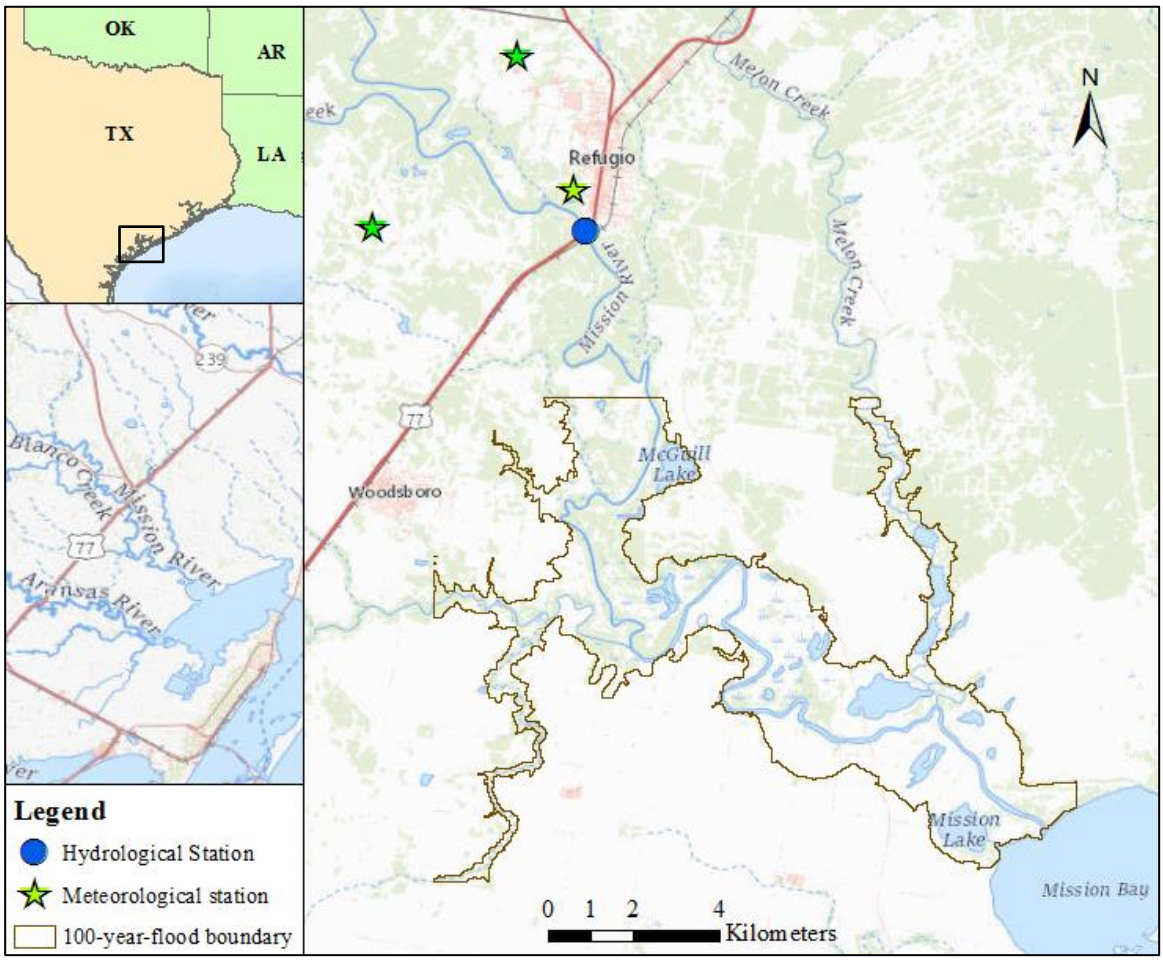

Fig. 1 Map of coastal region of the MRF within FEMA 100-year-flood boundary.

2.2 Datasets and preprocessing

Four types of data were used in this study: in situ measurements, satellite image data, land cover related products, and digital elevation model (DEM) derived products.

2.2.1 In situ measurements

The in situ measurements considered in this study include river discharge and precipitation data. The discharge data were acquired from a United States Geological Survey (USGS) gauge station (USGS 08189500) at Refugio, Texas, including daily mean discharge from water year 1984 to 2018. The discharge time series is shown in Fig. 2, in which discharge values at the date of Landsat images acquisition were highlighted.

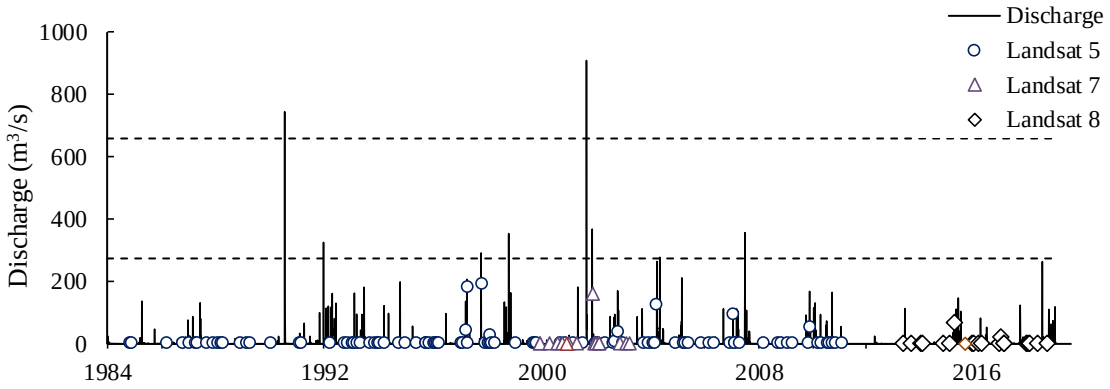

Fig. 2. River discharge from 1984 to 2018 and river discharge at the image acquisition date. Different color of dots represent images captured by Landsat 5, Landsat 7 and Landsat 8 satellite. The upper dash line represents 10-year-flood boundary, and the lower dash line represents 3-year-floood boundary.

The precipitation data were acquired from three National Oceanic and Atmospheric Administration (NOAA) meteorological station (USC00417529, USC00417533 and USC00417530) at Refugio, TX, including daily precipitation

measurements between 1984 and 2019. Both the river gauge station and the meteorological station were the closet stations of their respective types to the study area (Fig. 1). However, the precipitation data since August 2017 was not continuous.

2.2.2 Remotely sensed data

The satellite image data used in this study consisted of Landsat and PlanetScope images. The Landsat data included Landsat 5 TM, Landsat 7 ETM+, and Landsat 8 OLI images acquired between 1984 and 2018. We analyzed at total of 135 Landsat images (Table 1). The Landsat data used in this study were top-of-atmosphere (TOA) reflectance images, provided through and partially analyzed within Google Earth Engine (https://earthengine.google.com/). The spatial resolution of these Landsat images is 30 m, and the temporal resolution is 16 days. All Landsat images analyzed were cloud-free over water bodies. The acquisition time of each Landsat image was shown in Fig. 2.

The PlanetScope constellation is operated by Planet Company, which consists of more than 120 PlanetScope satellites (Planet Team, 2018). Most of the current satellite sensors are limited in providing water observations with both spatial and temporal consistency (Heimhumber, Tulbure, & Broich, 2018). However, PlanetScope data overcomes this obstacle. The high spatial resolution (3 m) and temporal resolution (daily) of PlanetScope imagery enables fine-scale dynamic monitoring of ground features. Previous studies (Houborg & McCabe, 2016; Cooley et al., 2017) have demonstrated the potential of PlanetScope data in monitoring changes in small water bodies. In this study, 2 cloud-free PlanetScope images were used to assess the accuracy of the water extents

extracted from the Landsat images. Inundation percentage derived from 18 PlanetScope images were used to validate the regression model of inundation created in section 4.2.

Table 1. Satellite Imagery Summary.

Sensor type	Numbers of images	Year	Spatial resolution (m)	Purpose
Landsat 5 TM	98	1984 - 2011	30	Inundation Analysis
Landsat 7 ETM+	16	1999 - 2003	30	Inundation Analysis
Landsat 8 OLI	21	2013 - 2018	30	Inundation Analysis
PlanetScope	18	2017 - 2019	3	Validation

2.2.3 Land cover related products

Land cover related products used in this study included soil classification data and land-cover classification data. The soil classification was obtained from the Web Soil Survey supported by the Natural Resources Conservation Service (NRCS) (https://websoilsurvey.sc.egov.usda.gov/App/WebSoilSurvey.aspx/). The soil classification map provided detailed information regarding soil, including composition, elevation, slope, depth, available water storage, permeability, etc. The dataset was jointly analyzed with the inundation frequency map to examine the spatial pattern of inundation.

The existing land-cover classification product used in this analysis was obtained from the Ecological Mapping Systems (EMS), generated by the Texas Parks and Wildlife Department (TPWD) (https://tpwd.texas.gov/landwater/land/programs/landscape-ecology/ems/). The spatial resolution of this classification map is 10 m, which combined

National Agriculture Imagery Program (NAIP) photographs, ground-reference data, enhanced satellite classification, landform-modeling efforts, and other ancillary data.

There are 42 land-cover classes within the MRF. We applied a class-merging operation to the classification map, reducing the number of land-cover classes from 42 to 13 classes. The major feature classes within this study included forest, woodland, shrubland, grassland, tidal/non-tidal wetland, open water, and anthropogenic. The merging process was based on the geographic position and ecological character of the feature classes. Because crops, urban area, and barren only dominated a few pixels, we merged these three classes to an anthropogenic class. The merging criterion for wetlands was based on whether such areas are influenced by tides. The class merging for vegetation was more complicated. First, we determined four categories: forest, woodland, shrubland, and grassland. Then, we determined several sub-classes within these four categories. The criterion was based on whether the vegetation belonged to evergreen or deciduous, as well as the geographic location of the vegetation. After class merging, the vegetation classes within the study area include mixed forest, hardwood forest, live oak forest, upland deciduous woodland, upland mesquite woodland, evergreen shrubland, deciduous shrubland and grassland. The last step was to assign each class into the categories listed above.

2.2.4 DEM derived products

The DEM data used in this study was obtained from the National Elevation Dataset (NED) released on December 4, 2012. NED was mainly derived from USGS 10-meter and 30-meter DEMs. The spatial resolution of NED varies depending on location. The

spatial resolution of NED for our study area is 1/3 arc-second (approximately 10 meters; United States Geological Survey, 2013). Slope can be defined as the rate of maximum change in z-value from each cell. The slope information was derived from NED through Slope function in ArcGIS 10.4. Due to the different spatial resolution between Landsat data and NED derived product, the DEM and slope data were resampled to 30 m, and then referenced to Landsat images.

3. METHODS

3.1 Extracting water pixels

The first step of deriving the inundation frequency map is to extract water pixels from satellite images. Among the most commonly-used water indices to extract water bodies from Landsat imagery are the Normalized Difference Water Index (NDWI) (McFEETERS, 1996) and the Modified Normalized Difference Water Index (MNDWI) (Xu, 2006). These two respective indices are calculated as follows:

$$NDWI = \frac{Green - NIR}{Green + NIR} \quad (1)$$

$$MNDWI = \frac{Green - MIR}{Green + MIR} \quad (2)$$

where Green is the green band, NIR is the near-infrared band, and MIR is the mid-infrared band. Compared to NDWI, MNDWI can better remove noise associated with built-up areas, vegetation, and soil, and MNDWI can generate higher water extraction accuracy than NDWI in most cases (Xu, 2006). Pixel values range from -1 to 1 after applying MNDWI, and a value of 0 has been suggested to be the default threshold for open waterbodies (Xu, 2016). However, waterbodies within the Mission River Floodplain (MRF) are much complicated, as they include wetlands, rivers, lakes, aquatic beds, and unconsolidated shore. Using a threshold of zero misses many details and underestimates the water-flooded extent (Ji et al., 2009; Huang et al., 2014).

The MNDWI threshold used for this study was -0.1. Setting of this threshold was based on the Landsat image-derived water-extraction results and visual interpretation of water in synchronous PlanetScope imagery, which has a spatial resolution of 3 m (Fig. 3(a) and (b)). Previous studies have also suggested -0.1 as the MNDWI threshold to use for extracting water from floodplain and wetland environments (Huang et al., 2014; Song et al., 2018). Thus, we applied a uniform threshold value of -0.1 to all Landsat image-derived MNDWI images over the 1984-2018 time period within the Google Earth Engine environment (Fig. 3(c) and (d)). To better ensure the accuracy of the water-extraction maps, visual inspection and manual editing was applied to remove/correct the misclassified pixels based on PlanetScope images.

PlanetScope imagery was used as the validation data source in this study. The most distinctive advantage of PlanetScope imagery is the 3 m spatial resolution and the daily revisit capability, which makes it a useful data source to validate the accuracy of Landsat-derived data products in this study. However, due to the poor radiometric quality introduced by the inexpensive sensors and the limited spectral resolution (Houborg & McCabe, 2016), it is difficult to accurately extract waterbodies from PlanetScope images using a constant threshold. Thus, approximate water boundaries within each PlanetScope image were derived by setting an upper threshold for the near-infrared band. The determination of the threshold was based on on-screen interpretation of the digital numbers (DNs) of most of the waterbodies in a given image. Then, manual delineation was implemented to modify the misclassified pixels (Fig. 3(c) and (d)). These steps were conducted for all the PlanetScope images used in this study.

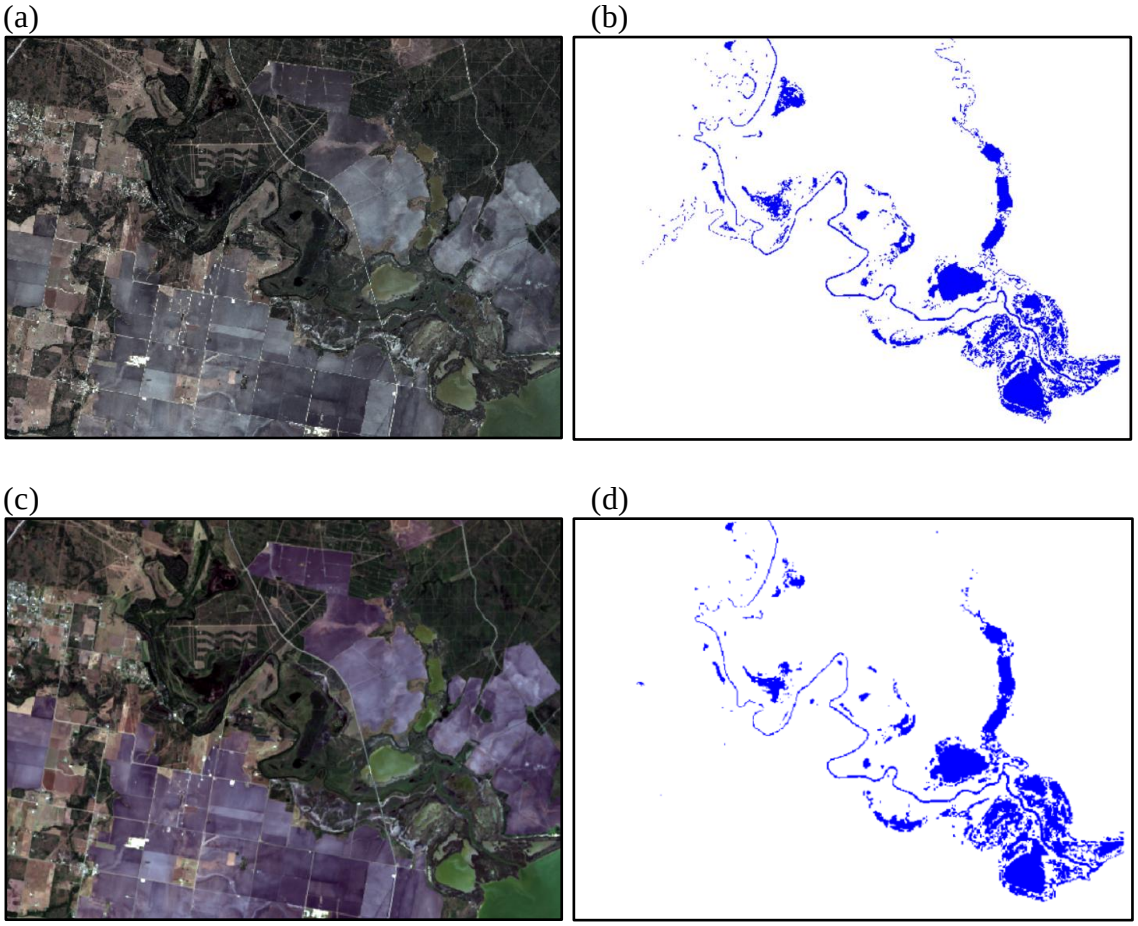

Fig. 3. (a) Landsat OLI image of the MRF; (b) water extraction from Landsat image using MNDWI; (c) PlanetScope image of the MRF; (d) water extraction from PlanetScope image using thresholding and manual editing. Note that both of the images were acquired on 12/09/2017, and the mean daily river flow was 0.15 m^3/s.

3.2 Deriving inundation frequency map

Accurate calculation for the inundation frequencies for all pixels based on Landsat observations is a significant part of deriving an inundation frequency map. Inundation frequency describes how often an area is submerged by the floodwater (Huang et al., 2014). For each pixel, inundation frequency is defined as the ratio of the number of observations in which detected as water to the number of total observations, which ranges

from 0 to 100 percent. For the imagery, this means that the inundation frequency is the counts of inundated time divided by all the Landsat observations within the study period. This approach is straightforward and easy to operate. Many previous studies have calculated inundation frequencies with this approach (Tulbure et al., 2016, Jin et al., 2017; Heimhuber et al, 2018). However, if we use all the available satellite observations to derive an inundation frequency map, we would face the problem that the temporal distribution of every available image is uneven, and the result can be temporal biased (i.e., more observations in dry season than that in wet season). Song et al. (2018) also mentioned this problem in their study. They assigned higher weights to the observations in pre-wet season, which had less cloud-free images than that in dry season. Thus, the water frequency map still could be biased in their study.

To solve this problem, we proposed a weighted approach to incorporate Landsat observations and gauge measurements. Daily flow time series from water year 1939 to 2018 were reordered from the lowest value to the highest value, and each discharge value was assigned with a rank starting from 1 to the largest value of discharge. The exceedance probabilities of the Mission River were calculated based on the instruction provided in a USGS report (U.S. Geological Survey., 2008), which is calculated as follows:

$$P = 100\frac{M}{N+1} \tag{3}$$

where P is the exceedance probability, M is the ranking position on the list, and N is the total number of daily mean flows. Exceedance probabilities were divided into 22 ranges, based on which the discharges were also divided into 22 ranges (Table 2).

Table 2. Calculations to derive the weights.

Flow conditions	Exceedance probabilities (P; %)	Discharge range (Q; m^3/s)	Number of flow data in the range (M_i)	Number of images in the range (N_i)	Weight (W_i)
Low flow	$P \geq 99$	$0 < Q \leq 3.0e\text{-}4$	320	2	0.56
	$95 \leq P < 99$	$3.0e\text{-}4 < Q \leq 9.4e\text{-}3$	1124	5	0.78
	$90 \leq P < 95$	$9.4e\text{-}3 < Q \leq 0.05$	1479	7	0.74
Dry conditions	$85 \leq P < 90$	$0.05 < Q \leq 0.07$	1465	2	2.55
	$80 \leq P < 85$	$0.07 < Q \leq 0.10$	1532	2	2.67
	$75 \leq P < 80$	$0.10 < Q \leq 0.12$	1426	2	2.48
	$70 \leq P < 75$	$0.12 < Q \leq 0.14$	1323	8	0.58
	$65 \leq P < 70$	$0.14 < Q \leq 0.17$	1445	11	0.46
	$60 \leq P < 65$	$0.17 < Q \leq 0.21$	1427	6	0.83
Mid-range flows	$55 \leq P < 60$	$0.21 < Q \leq 0.26$	1451	3	1.68
	$50 \leq P < 55$	$0.26 < Q \leq 0.31$	1675	8	0.73
	$45 \leq P < 50$	$0.31 < Q \leq 0.37$	1141	6	0.66
	$40 \leq P < 45$	$0.37 < Q \leq 0.45$	1565	9	0.61
Moist conditions	$35 \leq P < 40$	$0.45 < Q \leq 0.54$	1352	8	0.59
	$30 \leq P < 35$	$0.54 < Q \leq 0.65$	1526	8	0.66
	$25 \leq P < 30$	$0.65 < Q \leq 0.82$	1457	6	0.85
	$20 \leq P < 25$	$0.82 < Q \leq 1.08$	1401	11	0.44
	$15 \leq P < 20$	$1.08 < Q \leq 1.51$	1312	10	0.46
	$10 \leq P < 15$	$1.51 < Q \leq 2.72$	1450	8	0.63
High flow	$5 \leq P < 10$	$2.72 < Q \leq 7.94$	1424	2	2.48
	$1 \leq P < 5$	$7.94 < Q \leq 76.84$	1149	6	0.67
	$P < 1$	$Q > 76.84$	286	5	0.20

Each Landsat image was matched with a river discharge measured on the date of image-acquisition. The number of Landsat images falling in each range was calculated. Ideally, the number of Landsat images in a discharge range should be in proportional to the number of flow data in the same range. However, it is difficult to realize due to the availability of Landsat data. Thus, less weights should be assigned to the images in the range that received more number of observations than others, and vice versa. This means

weight is positively related to the number of flow data falling in each discharge range, but negatively related to the number of images falling in the range, which was calculated as:

$$Wi = \frac{Mi}{T} \cdot \frac{1}{Ni} \quad (4)$$

where Wi is the weight, Mi is the number of river flow data in the discharge range, Ni is the number of images in a discharge range, and T is the total number of river flow data. Inundation frequency was the stacking of each image timed the weights, which ranged from 0 to 100 percentage.

3.3 Analyzing relationships between inundation and discharge or precipitation

Quantifying the relationship between inundation extent and hydrological factors is essential to examine the long-term floodplain dynamics. Discharge is among the most important factors that influences the extent of floodplain inundation (Benke et al., 2000; Overton et al., 2009; ward et al., 2014). Benke et al (2000) built a linear regression model between gauge-measured discharge and inundation percentage estimated during flood events, and found a strong relationship between these two variables ($r^2 = 0.98$). However, previous studies found that there was a delay between measured increase in river discharge and subsequent inundation extent in the downstream, and the delayed time related to the scale of the floodplain (Overton et al., 2009; Huang et al., 2014). This means downstream region could be inundated several hours or few days after a flood event measured by a gauge station in the upstream. On the other hand, actual inundation extent would not decrease as rapidly as river discharge due to the retained water in residual pools (Benke et

al., 2000). Thus, the river discharge measured on the same day of image acquisition may not be appropriate to build regression model.

Consider the influence of the retained water after flood events, and the time lag between measured discharge and floodplain inundation, we calculated mean daily discharges of 1 to 15, 20, 25 and 30 days prior to the date of image acquisition. Linear regressions were built between mean daily discharges and inundation extents estimated from Landsat images. The coefficient of determination (r^2) of the regressions used to determine the discharge-inundation relationship.

Precipitation is a significant factor that influence floodplain inundation (Ward et al., 2014;Song et al., 2018). Both short-term and long-term cumulative precipitation will influence the percentage of water inundation (Jin et al., 2017). Short-term precipitation has direct impacts on floodplain inundation through surface water runoff. Long-term precipitation will affect the floodplain inundation through surface water storage in catchments and soil moisture (Jin et al., 2017). Same process was applied to cumulative precipitation data from 1 to 30 days to determine the precipitation-discharge relationship.

Because both discharge and precipitation will influence on the inundation extent, a multiple linear regression with two predictor variables (mean daily discharge and cumulative precipitation) was built. We used all combinations of mean discharge and accumulative precipitation with different time lags (1-15, 20, 25, 30 days) and inundation percentage to build regressions, which means 324 regressions in total were created. The regression with highest r^2 was selected as the model to predict inundation percentage based on mean discharge and cumulative precipitation.

3.4 Accuracy assessment

Two parts of accuracy assessment were included in this study. One was to assess the accuracy of the water-extraction maps from Landsat images. Influenced by the highly dynamic water extent in most floodplain environments, assessing the accuracy of inundation maps is more difficult relative to validating other remote-sensing products (Jin et al., 2017). To quantitatively assess the Landsat image-based water-extraction accuracy, two cloud-free, high-spatial-resolution PlanetScope images acquired at the date of Landsat images were selected as reference data. Cooley et al. (2017) found that PlanetScope images entail a positional error of <10 m RMSE. Thus, the PlanetScope images used in this study were georeferenced to synchronous Landsat images. Due to the different spatial resolutions of these two satellite data types, all Landsat images were spatially resampled to 3 m using nearest neighborhood method. Producer's accuracy and user's accuracy were calculated in order to assess the Landsat image-based water-extraction accuracy. Producer's accuracy represents how well the water bodies on the ground are classified in the Landsat imagery. User's accuracy represents how well the water pixels classified from Landsat imagery actually represents the water bodies on the ground (Congalton, 1991).

Another part of accuracy assessment was to validate the multiple linear regression model created in section 3.3. Inundation percentage of 18 PlanetScope images acquired between 2017 and 2019 were calculated. Cumulative precipitation of 5 days and mean discharge of 12 days prior to the PlanetScope image acquisition were calculated. Then, the inundation percentage was estimated using the regression model, and compared to the inundation percentage derived from the PlanetScope images.

4. RESULTS

4.1 Flood inundation frequency map

Fig. 4 showed the inundation frequency map of the Mission River Floodplain (MRF) over water year 1984 to 2018, which consisted of 135 scene of Landsat images with different weights. To better visualize the spatial pattern of inundation, the inundation map was divided into 10 ranges using the Geometrical Interval function in ArcGIS 10.4. The mean inundation frequency for the entire study area was 20.1%. After excluding open water bodies (rivers, lakes) from the map, the mean inundation frequency for the remaining area was 10.7%. It was observed that there was a gradient of increasing inundation frequency from the upstream of the Mission River to the coast. An area of 7.5 km^2 (17.7%) was never inundated after excluding open water bodies, most of which located in the upper portion of the study area. Only 5.5% of the area (2.3 km^2) was inundated more than 50% of the time over the period, most of which located at the mouth of the Mission River. It also showed that the area close to the main river channel had a relatively low inundation frequency comparing to the surrounding floodplain.

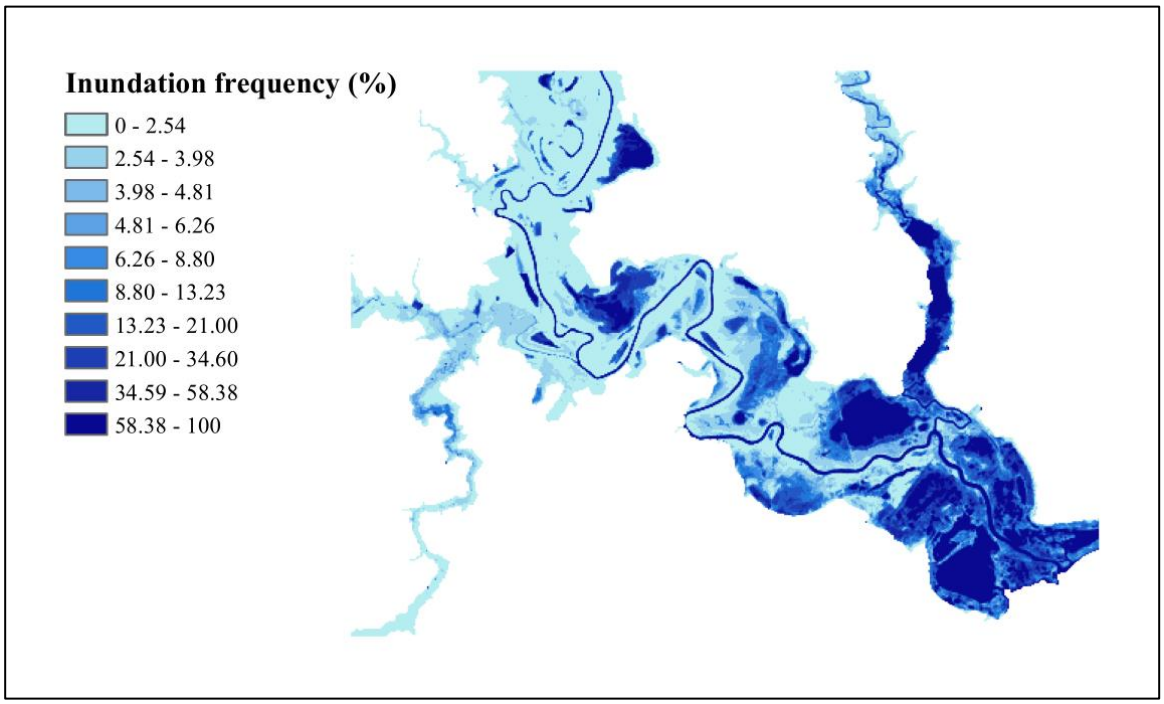

Fig. 4. Flood Inundation Frequency Map of the MRF.

Although the upstream of Mission River with high canopy-cover rate was not included in this study, the observation to the lower portion of the river floodplain was still influenced by vegetation. Optical sensors have limited ability of penetration and cannot see through the tree canopy, which means it is difficult to detect the water bodies under trees (Di Vittorio & Georgakakos., 2017). Radar has the major advantages of the good penetration capability, which means it can penetrate through clouds and tree canopy (Schumann & Moller., 2015). However, there was no available Radar data that could be used for long-term inundation monitoring (Heimhumber et al., 2018). Thus, the inundation frequency map derived in this study might underestimate the inundation frequency of the MRF.

4.2 Relationships between inundation and discharge or precipitation

Fig. 5(a) showed the coefficient of determination (r^2) of regressions between inundation percentage and mean discharge with different time lags. It was observed that there was a slightly increase in r^2 when the time lag increased from 1 to 4 days, and then the inundation-discharge relationship remained stable. All r^2 values were above 0.7 when calculating mean discharges from 2 to 15-day period. However, a relatively low r^2 was observed when using discharge on the same day of image acquisition. The reason was that there existed a delay between measured increase in river discharge and subsequent changes in inundation status (Overton et al., 2009; Huang et al., 2014). Thus, a low inundation percentage could be observed even if the gauge-measured discharge was high. The highest r^2 was obtained when discharge was calculated for an 11-day average (r^2 = 0.76). Then, the r^2 began to decrease when the time lags increased from 12 to 30 days, but inundation and discharge were still statistically correlated ($p < 0.05$; note that all the p values calculated in this thesis used t-test). It indicated calculating the mean discharge could provide a better estimation for inundation status, instead of applying the discharge value on the image-acquisition date.

Fig. 5(b) showed the r^2 of regressions between inundation percentage and cumulative precipitation with different time lags. There was no relationship (r^2 = 0.07 and 0.13, respectively; $P > 0.05$) between inundation and precipitation when cumulative precipitation was calculated for 1 and 2 days. However, a strong relationship between inundation and precipitation was observed when the time lag increased to 3 day. This means precipitation will not led to stagnant water within a relatively short period (less

than 3 days). The highest r^2 (0.70) was attained when calculating cumulative precipitation for a period of 5 days. Although r^2 sustained decreased when calculating time lags for precipitation from 11 to 30 days, precipitation still exhibited a statistically significant influence on inundation percentage ($r^2 > 0.4$, $p < 0.05$). This result corresponded to the findings in a previous study (Jin et al., 2014), in which the authors stated both short-term and long-term precipitation would influence the inundation status, and the strongest inundation-precipitation relationship was obtained with 5-day cumulative precipitation.

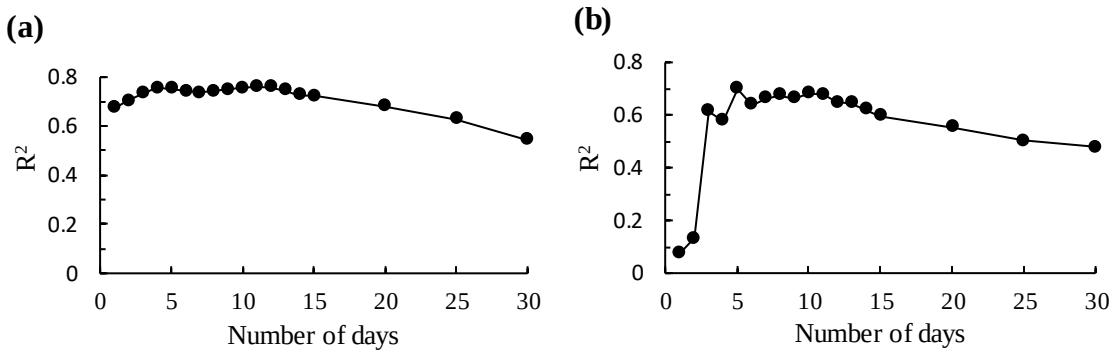

Fig. 5. (a) Coefficient of determination (r^2) of the linear regressions between inundation percentage and mean discharge with different time lags; (b) r^2 of the linear regressions between inundation percentage and cumulative precipitation with different time lags.

It was demonstrated that both discharge and precipitation within certain periods were statistically significant to inundation percentage. Regression models were established to predict inundation percentage in previous studies (Benke et al., 2000; Gibbs et al., 2016). However, they only considered discharge as the independent variable for the regression. In this study, no linear regression between inundation extent and discharge or precipitation exhibited a relationship with r^2 greater than 0.8. With the multiple linear

regressions built in section 3.3, it suggested that using both mean discharge and cumulative precipitation as the inputs generated better result for inundation estimation. It turned that the highest r^2 was from the regression model with 12-day mean daily discharge and 5-day cumulative precipitation as the inputs (Fig. 6). The regression model was expressed as:

$$y = 0.18x_1 + 0.50x_2 + 16.63 \quad (5)$$

where y is inundation percentage, x_1 is cumulative precipitation of 5 days (mm), and x_2 is mean daily discharge of 12 days (m^3/s).

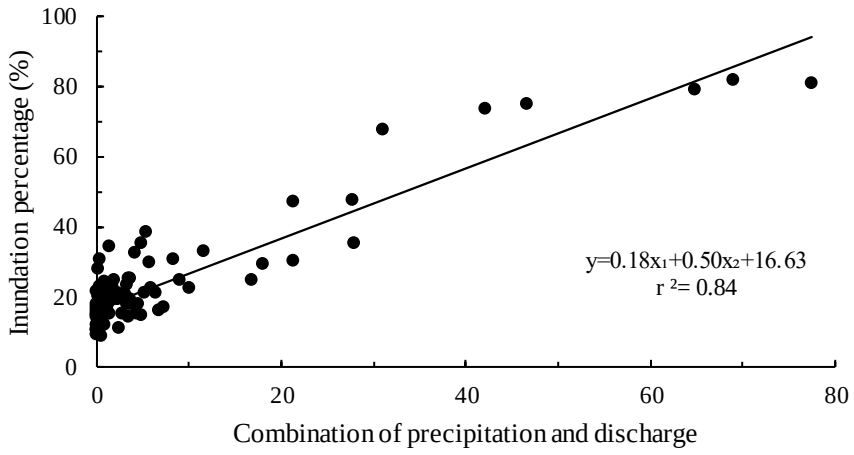

Fig. 6. Multiple linear regression between inundation percentage ($\boldsymbol{y}$), 5-day cumulative precipitation ($\boldsymbol{x_1}$), and 12-day mean daily discharge ($\boldsymbol{x_2}$).

4.3 Long-term inundation time series

Given the relationship between mean discharge, cumulative precipitation and inundation extent (Fig. 7), long-term inundation dynamics of the MRF were constructed

based on gauge-measured hydrological and metrological data from Jan 12, 1984 to July 31, 2017 (Fig. 7). Results indicated that the temporal distribution of flood inundation varied greatly from year to year. Floods led to >50% inundation occurred 172 days over the period, which means >50% of the floodplain would be inundated for about 5 days in a year. During the wet year of 1990, 1993, 1997, 1998, 2001, 2004 and 2007, the floods with >50% area inundated exceed 10 days. However, there were 19 years within the 34-year period receiving no flood events that led to >50% inundation.

The most significant drought event occurred between 2011 and 2014. No flood event led to >50% inundation during this period. Result showed the mean inundation percentage between 2011 and 2014 was only 18.3%, and the mean inundation percentage for the 34-year period was 21.3%. There were other drought events with shorter duration, which were from 1984 to 1985, 1988 to 1989, and 1999 to 2000. No significant flood was observed during these periods. Fig. 7 also reflected the periods with extensive flood events. For example, from August 31 to November 28 in 2001, the floodplain received >50% inundation for 26 days during the 90-day period, and the mean inundation percentage was 41.1%. Severe drought and frequent flood events could lead to significant ecological effects to both flora and fauna communities with in the floodplain. The long-term inundation dynamics enabled us to determine the distribution and duration of these events.

Responses of floodplain wetlands are significant to sustainable water resources protection and management. How floodplain responses to flood events with different magnitudes needs to be better understood and quantified (Di Vittorio & Georgakakos.,

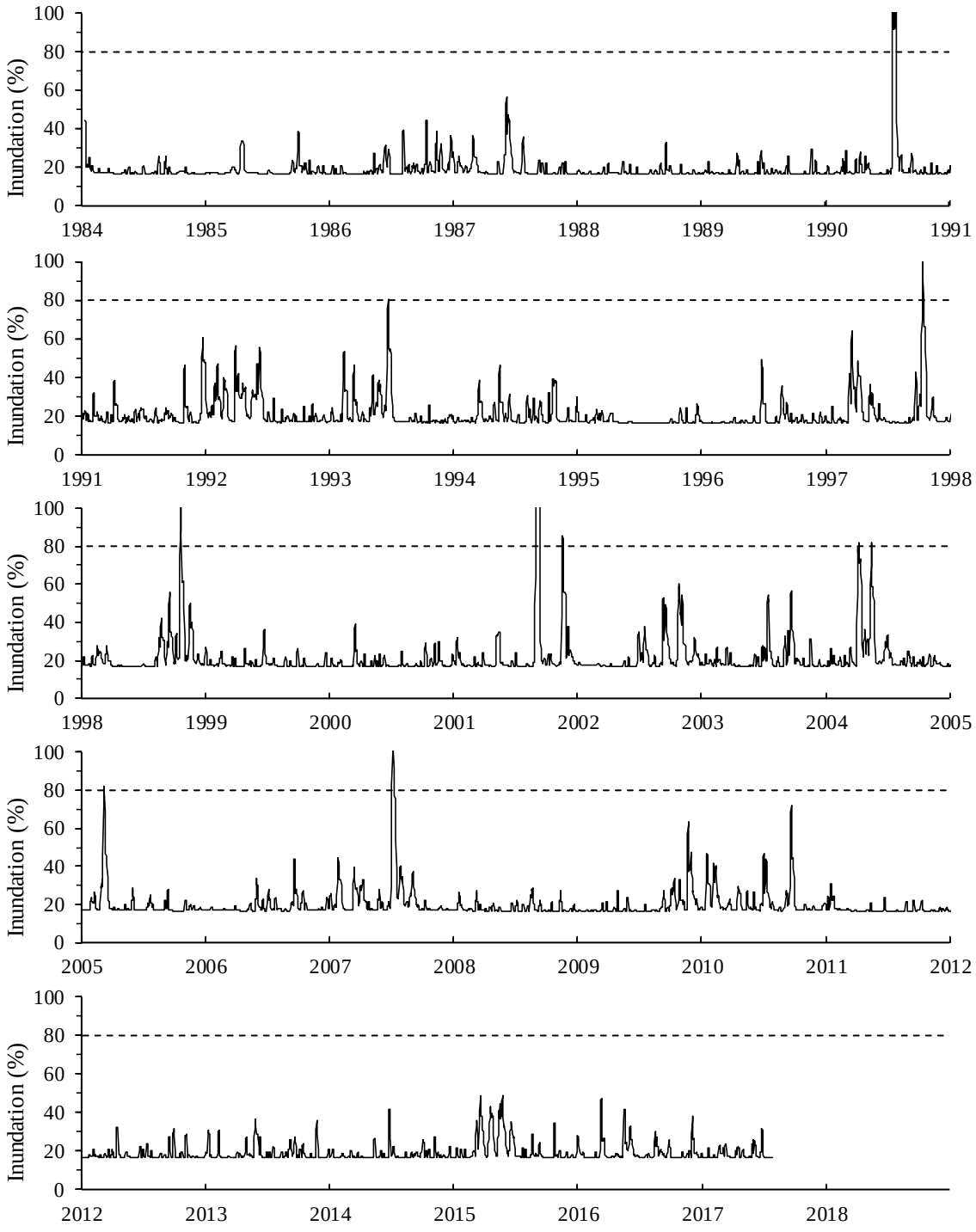

Fig. 7. Predicted floodplain inundation percentage from January 12, 1984 to July 31, 2017. The dash lines indicate 80% inundation, above which the predicted inundation percentage is less reliable.

2017). Banke et al. (2000) indicated that floodwater on the surfaces of floodplain could create new habitats and provide the chance for material exchange between living and nonliving matter. Thus, understanding the inundation dynamics of floodplains over long timeframes is essential to examine how both flora and fauna communities adapt to the wet-dry transition environment (Thomas et al., 2011).

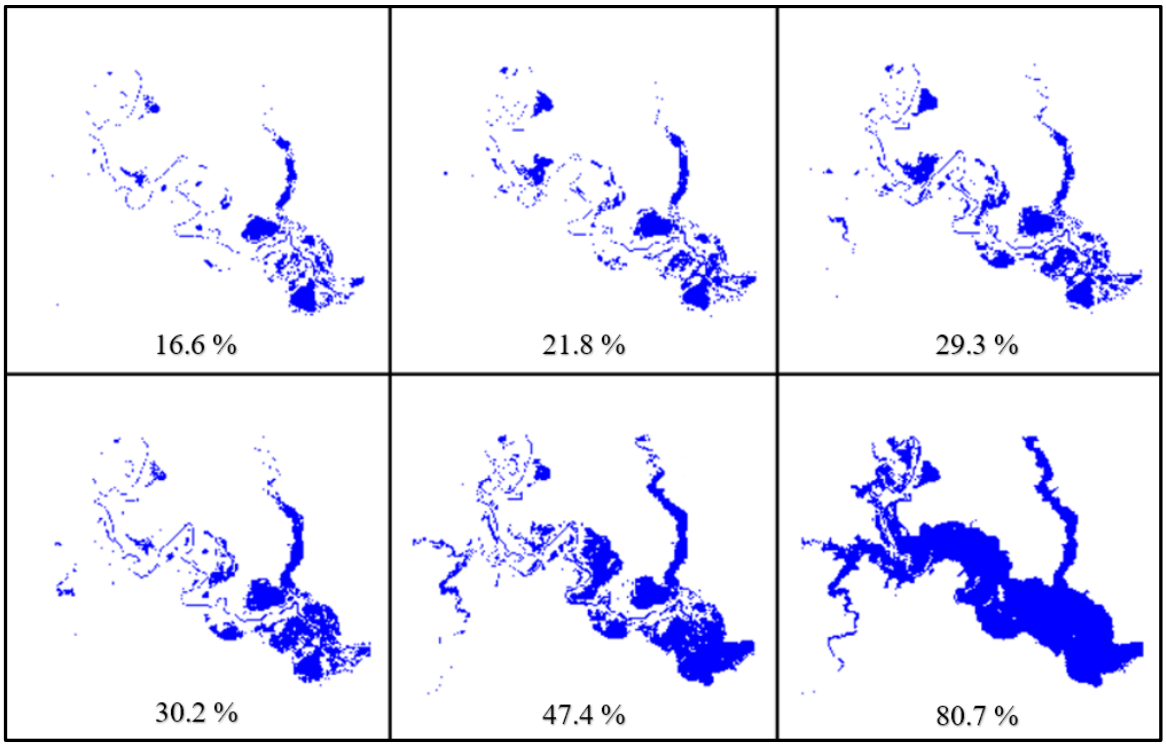

Fig. 8. Relationship between inundation percentage and inundation extent. The numbers in the figure refer to the inundation percentage. The inundation extents were extracted from Landsat images using MNDWI.

The strong relationship between mean discharge, cumulative precipitation and inundation extent (Fig. 7) enabled us to determine the inundation percentage within the MRF. It is also essential to transfer the inundation percentage to the spatial distribution of

actual inundated area. In section 3.1, the water extents of 135 Landsat images were extracted. If the inundation percentage within the floodplain is calculated, the Landsat images with closest inundation percentage could be selected to estimate the inundated area (Fig. 8).

4.4 Accuracy assessment results

4.4.1 Accuracy assessment for water extraction results

The quantitative accuracy assessment for the two groups of images acquired on different days reveals similar accuracy (Table 3). The user's accuracies of water extraction (71.3% and 70.3%) were lower compared to the producer's accuracies (82.8% and 85.7%). The difference between these two accuracies could be due to the scaling issues. The width of the upstream zone and tributaries of Mission River are less than 30 meters. There are many small ponds and wetlands within the study area, and their sizes are less than the pixels size of Landsat imagery. These small water bodies (narrow channels, small ponds) could be more accurately captured by PlanetScope images compared to Landsat images. However, because of the low threshold (-0.1) we applied to the MNDWI results, many small water bodies could also be captured by Landsat image. Thus, the Landsat images could slightly overestimate the extent of water bodies compared to PlanetScope images.

Table 3. Classification accuracy-assessment results for Landsat image-based water extraction, with PlanetScope image-derived water areas used as reference.

Date	Producer's Accuracy	User's Accuracy
12/09/2017	82.8%	71.3%
08/22/2018	85.7%	70.3%

Fig. 9 revealed that the lakes and main channels could be captured by both PlanetScope and Landsat images. The main inconsistency of the result came from the small ponds and wetlands along the downstream of the Mission River, which was overestimated by the Landsat images (yellow region). The red region in Fig. 9 indicated that the upstream and tributaries of the Mission River was too narrow to be captured by Landsat images. However, the accuracy assessment results still indicate that Landsat images could extract most of the water bodies within the MRF with a high accuracy.

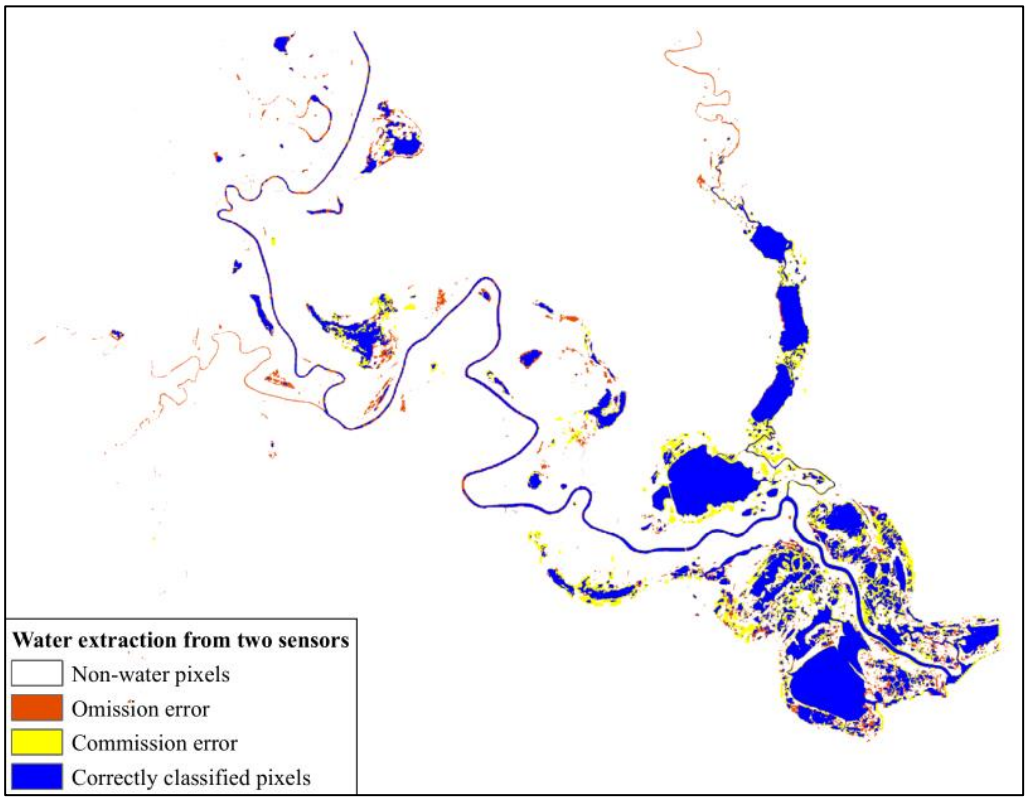

Fig. 9. Comparison of water-extraction results of Landsat and PlanetScope images. Both of the satellite images used in this analysis were acquired on 12/09/2017.

4.4.2 Accuracy assessment for regression model of inundation

Fig. 10 showed the comparison of actual inundation percentage calculated from digitization of PlanetScope images and model-derived inundation percentage. It turned that all of the prediction errors were less than 5% in absolute value. The root mean square error (RMSE) was 2.9%. This result indicated that the multiple linear regression model created in this study provided accurate estimations over inundation percentage. This model took both precipitation and discharge into consideration, and generated better prediction accuracy than using one of these variables. However, the model could not provide accurate prediction of inundation percentage for some dates with extreme low or high inundation percentage but normal discharge or precipitation condition. Tide was a factor that lead to temporal increase in inundation extent (Jin et al., 2017). However, there were no tidal station within this area. Thus, measured tidal data could not been incorporated in the regression model of inundation to determine the effects caused by tides.

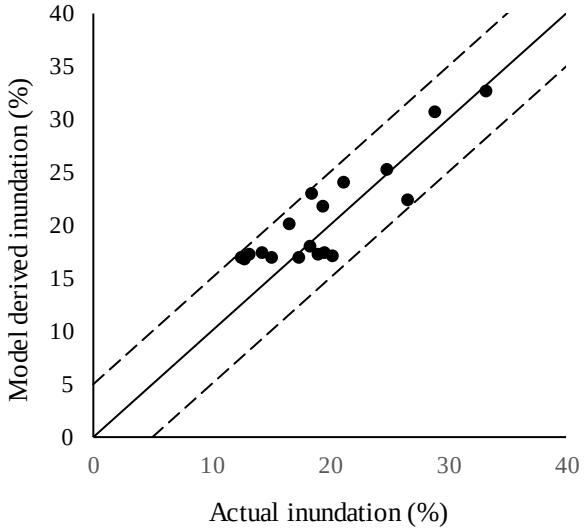

Fig. 10. Comparison of actual inundation percentage obtained from the digitization of PlanetScope images and model-derived inundation percentage. The solid line presents perfect match between derived and actual inundation. The two dashed lines indicates the boundaries of 5% error.

5. DATA ANALYSIS AND DISCUSSION

5.1 Soil

Soil type is a significant factor that affects the surface water inundation. The characters of soil, including permeability, water storage capacity, slope, directly influences the retaining of groundwater. Jin et al (2017) found that soil saturation was important to determine the provision of wetland systems, and the difference in soil properties could lead to different inundation pattern. However, they did not quantitatively examine the relationship between soil types and inundation pattern. Many previous studies (Chen et al., 2014; Ward et al., 2014; Tulbure et al., 2016; Jin et al., 2017) have related inundation frequency with land-cover types and wetland types. However, none of them analyzed the relationship between inundation frequency and soil types.

A soil classification map from NRCS was used to examine the relationship between soil types and inundation frequency. The NRCS soil map was overlaid and clipped to the extent of the inundation frequency map (Fig. 11). Minimum score, lower quartile, median, upper quartile, maximum score and whiskers were calculated for each soil type, based on which a box plot was created to provide the summary of the inundation frequencies of soil types (Fig. 12). The mean inundation frequency was also calculated with respect to each type of soil by averaging the inundation frequency in the polygon of each soil type based on the inundation frequency map.

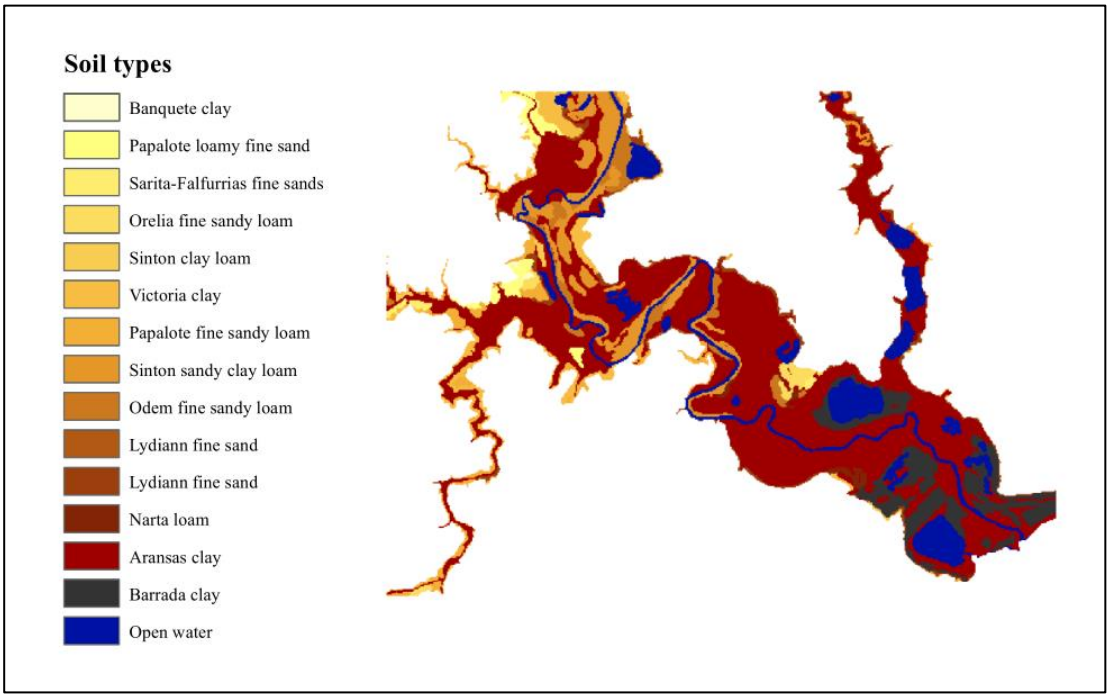

Fig. 11. Natural Resources Conservation Service (NRCS) soil type map of the Mission River Floodplain (MRF). The soil classes were reordered from the lowest to the highest based on their inundation frequencies.

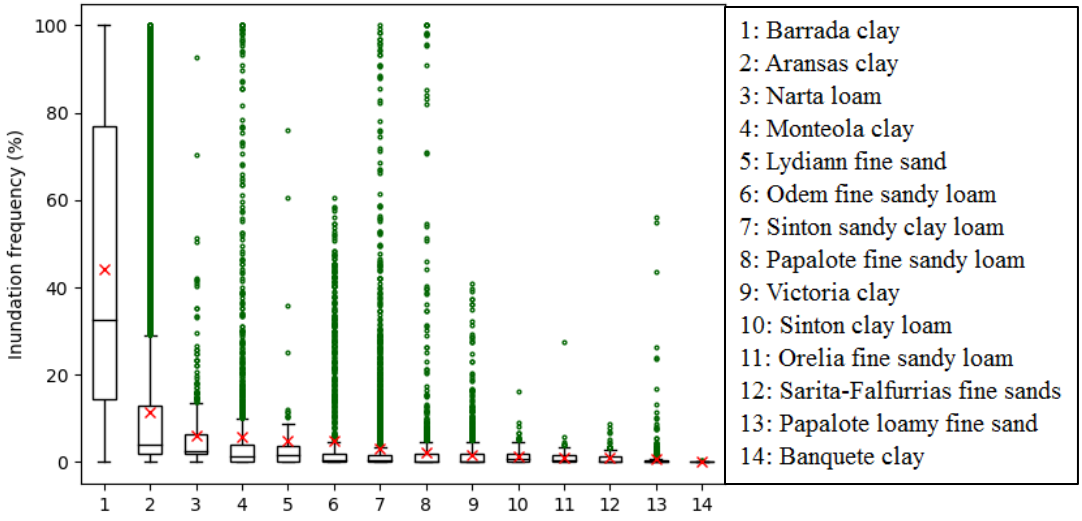

Fig. 12. Box plot of the inundation frequency associated with each soil class. Note that 'x' symbol in all graphics of this thesis represents mean value of a certain class.

Barrada clay obtained the highest mean inundation frequency (44.5%). Most of the Barrada clay located in the wetlands close to the coast. Aransas clay was the dominant type of soil within the MRF, accounting for 56.3% of the area. The mean inundation frequency of Aransas clay was 11.5%. Fig. 12 shown that Aransas clay had many outlies shown in the box plot, indicating that although most of Aransas clay distributed in the regions that were not inundated frequently, some could located in the region received intensive floods. Other types of soil were associated with inundation frequencies ranging from 0.03% to 6.4%. It turned that the types of soil with relatively low inundation frequency were distributed along the upper portion of the riverbank, which was corresponding to the area that seldom got flooded (Fig. 4). However, some pixels within these types of soil still possessed high inundation frequencies. The main reason was due to the pixel size. More than one types of soil could exist in the extent of a pixel, but we could only assign one type of soil to the pixel. It also revealed that the region with high concentration of clay usually exhibited higher inundation frequency compared to sandy and loamy soil.

Result indicated that the variance in flood inundation frequency was closely related to the different properties of soil. Great differences in soil properties could occur within a small geographical area, leading to the variance in the spatial pattern of inundation. The differences in soil properties could directly influence the stagnant time of floodwater (Gibbs et al., 2016). Rafael et al. (2018) found that flooding could induce changes to the composition of the soil microbial community, and extreme flood events would reduce the functioning of soil. The different duration of floodwater would lead to the variance in soil

condition. Vegetation within in different soil conditions responds to the flood inundation diversely (Wong et al., 2015). This means the flood inundation and soil is in a process of mutual influence. Thus, it is essential to examine the relation between soil and flood inundation in order to optimize the utilization of land with different soil types.

5.2 Land cover

Previous studies have recognized the ecological and environmental importance of floodplain and wetland inundation (Benke et al., 2000; Chen et al., 2013; Huang et al., 2014). Relating inundation dynamics with land-cover types is essential to analyze the influence of inundation dynamics instead of only monitoring the changes in water extent (Chen et al. 2014). Most of biological productions and organic matters within floodplains are from the lateral exchange of river-floodplain systems (Junk et al., 1989). Several studies indicated that vegetation type and health condition was dependent on flood inundation frequency (Bren & Gibbs., 1986; Tockner et al., 2000). Examining the relationship between distribution of land-cover types and flood inundation frequency provides insights into the functioning of the river-floodplain ecosystem (Benke et al., 2000).

A reclassified land-cover map from EMS was jointly analyzed with the inundation frequency map to examine the ecological impacts of flood inundation. The process to obtain the reclassified land-cover map was provided in section 2.2.3. The land-cover map was clipped to the same extent of the inundation frequency map, and the 13 land-cover classes were reordered from the lowest to the highest based on their inundation frequencies

(Fig. 13). Then, a box plot indicating the inundation frequency of each land-cover type was created (Fig. 14).

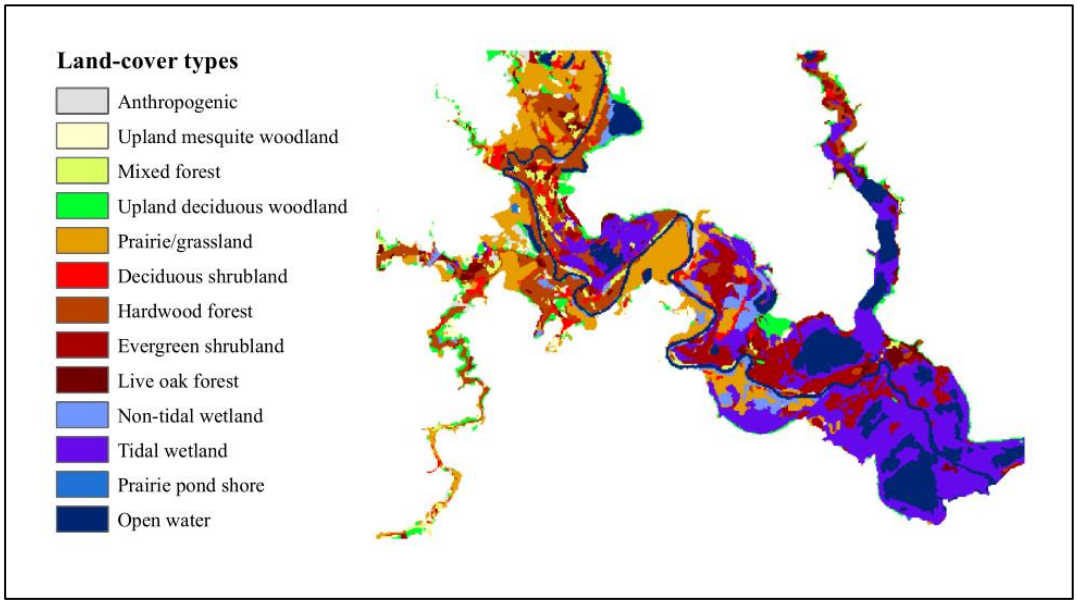

Fig. 13. Ecological Mapping System (EMS) land-cover classification of the MRF. The land-cover classes were reordered from the lowest to the highest based on their inundation frequencies.

Result showed that the land-cover type with the highest mean inundation frequency was prairie pond shore (30.6%), and the inundation frequency of prairie pond shore varied from locations to locations (Fig. 13). The mean inundation frequency of tidal wetland was 21.7%, which was higher than that of non-tidal wetland (15.3%). It suggested that tide could be an important factor that influenced the floodplain inundation. Among all the vegetation classes, live oak forest possessed the highest mean inundation frequency (7.4%), and upland mesquite woodland was associated with the lowest mean inundation frequency (1.7%). Mesquites are desert adapted, drought tolerant trees. Their distribution

indicated that they preferred to live in the environments that were seldom inundated. The anthropogenic class processed the lowest mean inundation frequency (1.4%), which consisted of cropland and urban area with low intensity. Fig. 13 also showed that the anthropogenic class had less outliers than that of other land-cover types.

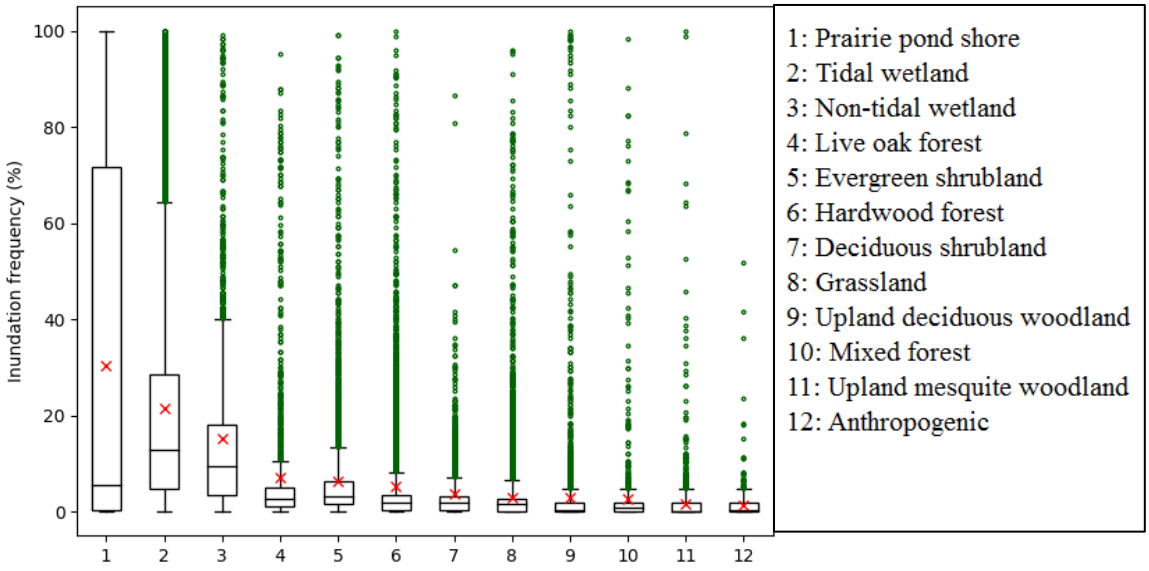

Fig. 14. Box plot of the inundation frequency associated with each land-cover type.

In the MRF, evergreen vegetation included live oak forest and evergreen shrubland. Deciduous included hardwood forest, deciduous shrubland, upland deciduous woodland and upland mesquite woodland. Result showed that the mean inundation frequency associated with live oak forest and evergreen shrubland were higher than other vegetation types, which were 7.4% and 6.6%, respectively. Then, the mean inundation frequencies of evergreen and deciduous were calculated. Result exhibited that the mean inundation frequency associated with evergreen and deciduous was 6.7% and 4.0%,

separately. The mean inundation frequency of grassland was 3.2%, which was lower than that of both evergreen and deciduous. It revealed more frequent inundation was usually associated with evergreen comparing to deciduous and grassland.

Examining how different types of vegetation adapt to floods is essential to understand the natural properties of floodplain ecosystems. Jin et al., (2017) found that wetlands with deciduous or evergreen forest and scrub exhibits less frequent floods inundation compared to emergent, which meant that the existence of vegetation would influence the duration of floods. The structural characteristic of vegetation in aquatic environments influences light penetration, as well as the habitats for submerged plant and algae (Ward et al., 2014). The frequency of floods inundation could also influence the suspended sediment concentration, and hence affects the productively of the vegetation (Han et al., 2015). The predicted inundation frequency can be used to determine how floods with changing frequencies affect different communities, especially flood-dependent vegetation and animals (Thomas et al., 2011). Thus, it is necessary to relate floodplain inundation frequency with different vegetation types to determine their relationship among different ecosystems.

5.3 Elevation

Many previous studies used digital elevation model (DEM) to map inundation extent of floodplain environments (Gibbs et al., 2016; Heimhuber et al., 2018), or improve the mapping accuracy of surface water (Feyisa et al., 2014). In this study, DEM derived from the National Elevation Dataset (NED) was jointly analyzed with the inundation frequency map to examine the relationship between inundation frequency and elevation.

The DEM exhibited an obvious falling gradient from the upstream to the coast (Fig. 15). To quantitatively analyze the influence of elevation on inundation frequency, the DEM was reclassified to 11 ranges with an interval of 1 m. Considering the influence of open water bodies, all the rivers, lakes and ponds were masked when examining the relationship between inundation frequency and elevation. Then, a box plot was created based on the statistics for the 11 ranges. The mean inundation frequency of each range was also calculated (Fig. 16).

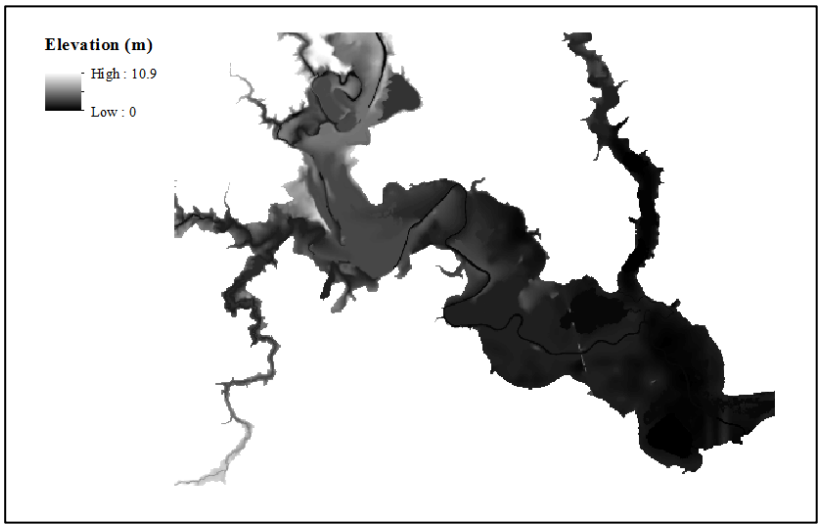

Fig. 15. Digital elevation model (DEM) of the MRF derived from the National Elevation Dataset (NED).

Fig. 16 indicated that elevation was a significant factor that caused the variance in inundation frequency. The mean inundation frequency was 44.0% when elevation was below 1 m. However, mean inundation frequency decreased dramatically along with the increasing of elevation. The mean inundation frequency dropped to 11.8% when the elevation range rose to 1-2 m. When the elevation was above 8 m, the mean inundation

frequency dropped below 1%. It also exhibited that when elevation was below 1 m, inundation frequencies varied from locations to locations. The inundation frequencies of 50% of the floodplain area ranged from 0 to 11.0% or 84.7% to 100% within this elevation range. The variations in inundation frequency decreased along with the increasing elevation.

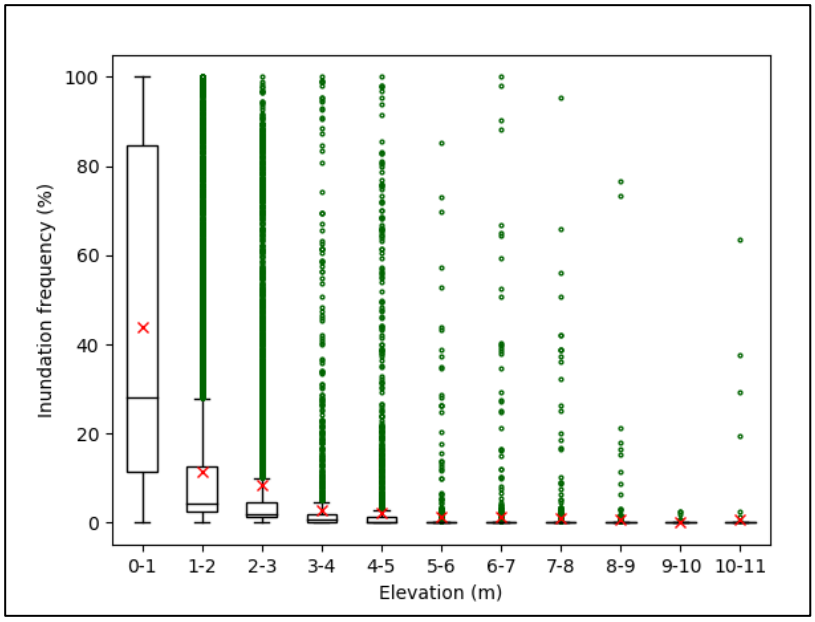

Fig. 16. Box plot of the inundation frequencies associated with different elevation ranges. The DEM was derived from the National Elevation Dataset (NED).

5.4 Slope

Slope can be defined as the rate of maximum change in z-value from each cell. Margono et al (2014) used slope as one of the explanatory variables to map per-pixel wetland probability, and found that slope was an important variable in mapping wetlands. Tulbure et al (2016) used slope to stratify the area by not allowing water to occur in area

with steep slopes, for water is difficult to retain in the steep slopes. In this study, slope derived from NED through the Slope function in ArcGIS 10.4 and was jointly analyzed with the inundation frequency map to further examine their relationship (Fig. 17). The slope map was reclassified to 10 ranges using the Geometrical Interval function in ArcGIS 10.4. All the water bodies were masked using the same water mask in 5.3. Then, a box plot was created based on the statistics of the 10 ranges (Fig. 18).

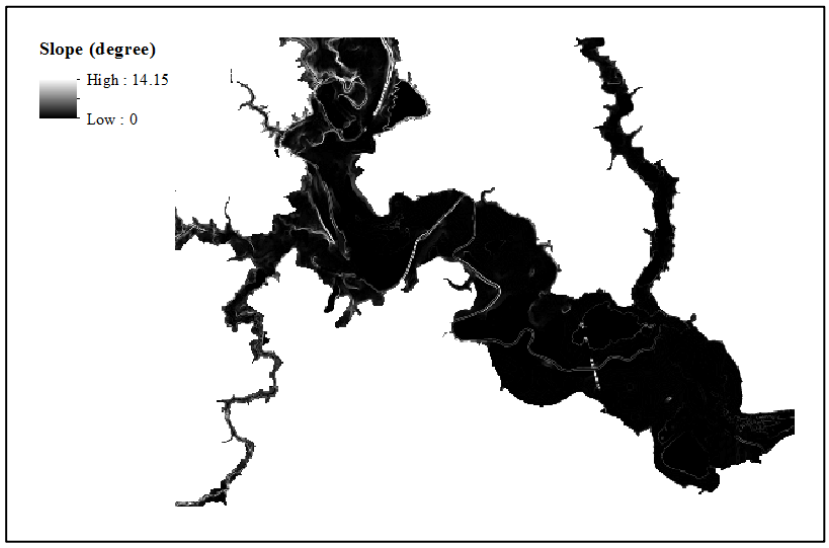

Fig. 17. Slope of the MRF derived from NED.

Fig. 18 revealed that the range with lowest slope received more frequent inundation than other ranges. The median value of each range exhibited a decreasing trend along with the increasing of the slope. However, the mean value of each range did not exhibited the same trend. The lowest mean inundation frequency was associated with the slope ranging from 3.8 to 4.9 degree, which was 3.8%. Then the mean inundation frequency began to rise with the increasing of slope. The mean inundation frequency

reached 9.9% when slope was between 8.2 and 14.2 degree. This means many pixels with high inundation frequency fell into this range, leading to the low median but high mean value. This phenomenon could be due to the 30 m-spatial resolution of the data. For a great number of pixels with high slope value distributed along the Mission River, and these pixels were always associated with high inundation frequencies (Fig. 17). Given the relationship between median inundation frequency and slope, it still revealed that the increase in slope lead to the decrease in inundation frequency. However, this relationship was not as strong as that between elevation and inundation frequency (Fig. 16).

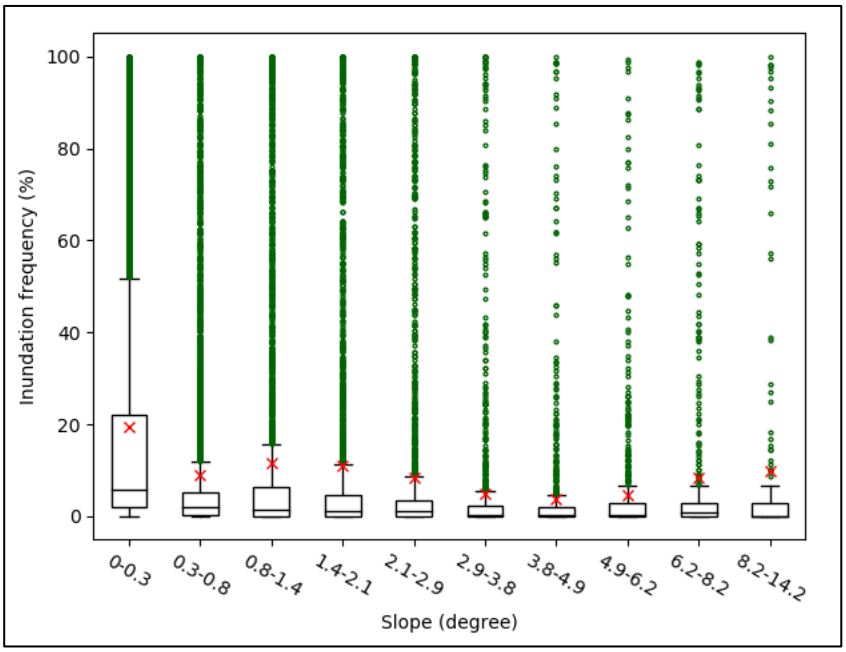

Fig. 18. Box plot of the inundation frequencies associated with different slope ranges. The slope was derived from NED.

6. SUMMARY AND CONCLUSIONS

This study proposed a weighted approach to create an inundation frequency map of the Mission River Floodplain (MRF) combining Landsat images ranging from 1984 to 2018 and long-term gauge measurements. This approach assigned different weights to images to reduce the temporal bias of observations, which was also applicable to inundation frequency analysis of other rivers. A multiple linear regression was created, which used cumulative precipitation and mean discharge as predictor variables. The long-term inundation dynamics of the MRF were determine through the regression model. To examine the relationship between inundation frequency and relevant factors, data layers including soil types, land-cover types, elevation and slope were jointly analyzed with the inundation frequency map. Followings are the main findings of this study:

(1) A multiple linear regression provided more accurate estimation of inundation percentage than linear regression with only one variable, in which cumulative precipitation of 5 days and mean discharge of 12 days were used as the predictor variables ($r^2 = 0.84$).

(2) Soil types, land-cover types, elevation and slope revealed strong relationships with inundation frequency. Clay usually exhibited higher inundation frequency compared to sandy and loamy soil, and more frequent inundation was associated with evergreen comparing to deciduous and grassland. Inundation frequency decreased along with the increase in both elevation and slope. However, this phenomenon was less obvious in slope than elevation.

The derived inundation frequency map and long-term inundation dynamics provide insights into the spatio-temporal patterns of flood inundation over the MRF. Such information is significant to the protection and restoration of river-floodplain ecosystems, and provides a key to the healthy functioning and sustainable development of these systems. The findings can also assist in understanding the relationship between the inundation dynamics and floodplain ecology of other unregulated coastal rivers.

REFERENCES

Alsdorf, D., Rodriguez, E., Lettenmaier, D. P. (2007). Measuring surface water from space. Rev. Geophys 45, 1–24.

Benke, A. C., Chaubey, I., Ward, G. M., & Dunn, E. L. (2000). Flood pulse dynamics of an unregulated river floodplain in the southeastern U.S. coastal plain. Ecology, 81(10), 2730-2741.

BobÉE, B. (1975). The log pearson type 3 distribution and its application in hydrology. Water Resources Research, 11(5), 681-689.

Bren, L. J., & Gibbs, N. L. (1986). Relationships between flood frequency, vegetation and topography in a river red gum forest. Australian Forest Research, 16(4), 357-370

Chen, Y., Huang, C., Ticehurst, C., Merrin, L., & Thew, P. (2013). An evaluation of MODIS daily and 8-day composite products for floodplain and wetland inundation mapping. Wetlands, 33(5), 823-835.

Chen, L., Jin, Z., Michishita, R., Cai, J., Yue, T., & Chen, B. (2014). Dynamic monitoring of wetland cover changes using time-series remote sensing imagery. Ecological Informatics, 24, 17-26.

Chormanski, J., Okruszko, T., Ignar, S., Batelaan, O., Rebel, K. T., & Wassen, M. J. (2011). Flood mapping with remote sensing and hydrochemistry: a new method to distinguish the origin of flood water during floods. Ecological Engineering, 37(9), 1334-1349.

Cooley, S. W., Smith, L. C., Stepan, L., & Mascaro, J. (2017). Tracking Dynamic Northern Surface Water Changes with High-Frequency Planet CubeSat Imagery. Remote Sens. 9, 1306.

Congalton, R. G. (1991). A review of assessing the accuracy of classifications of remotely sensed data. Remote Sensing of Environment, 37(2), 270-9.

Di Vittorio, C. A., & Georgakakos, A. P. (2017). Land cover classification and wetland inundation mapping using modis. Remote Sensing of Environment, 204, 1-17.

Feyisa, G. L., Meilby, H., Fensholt, R., & Proud, S. R. (2014). Automated water extraction index: a new technique for surface water mapping using Landsat imagery. Remote Sensing of Environment, 140(1), 23-35.

Gibbs, M. S., Clarke, K., & Taylor, B. (2016). Linking spatial inundation indicators and hydrological modelling to improve assessment of inundation extent. Ecological Indicators, 60, 1298-1308.

Halabisky, M., Moskal, L. M., Gillespie, A., & Hannam, M. (2016). Reconstructing semi-arid wetland surface water dynamics through spectral mixture analysis of a time series of Landsat satellite images (1984–2011). Remote Sensing of Environment, 177, 171-183.

Han, X., Chen, X., & Feng, L. (2015). Four decades of winter wetland changes in Poyang Lake based on Landsat observations between 1973 and 2013. Remote Sensing of Environment, 156, 426-437.

Heimhuber, V., Tulbure, M. G., and Broich, M. (2018). Addressing spatio-temporal resolution constraints in Landsat and MODIS-based mapping of large-scale floodplain inundation dynamics. Remote Sensing of Environment 211 (2018) 307–320.

Houborg, R., McCabe, M. F. (2016). High-Resolution NDVI from Planet's constellation of earth observing Nano-satellites: A new data source for precision agriculture. Remote Sens., 8, 768.

Huang, C., Wu, J., Chen, Y., & Yu, J. (2012). Detecting floodplain inundation frequency using MODIS time-series imagery. Agro-Geoinformatics (Agro-Geoinformatics), 2012 First International Conference on. IEEE.

Huang, C., Chen, Y., & Wu, J. (2014). Mapping spatio-temporal flood inundation dynamics at large river basin scale using time-series flow data and Modis imagery. International Journal of Applied Earth Observation and Geoinformation, 26, 350-362.

Hui, F., Xu, B., Huang, H., Yu, Q., & Gong, P. (2008). Modeling spatial-temporal change of Poyang Lake using multi-temporal Landsat imagery. International Journal of Remote Sensing, 29(20), 5767-5784

Ji, L., Zhang, L., Wylie, B., 2009. Analysis of dynamic thresholds for the normalized difference water index. Photogrammetric Engineering & Remote Sensing, 75(11), 1307-1317.

Jin, H., Huang, C., Lang, M. W., Yeo, I. Y., & Stehman, S. V. (2017). Monitoring of wetland inundation dynamics in the Delmarva Peninsula using Landsat time-series imagery from 1985 to 2011. Remote Sensing of Environment, 190, 26-41.

Junk, W.J., Bayley, P.B. and Sparks, R.E. (1989). The flood-pulse concept in river-floodplain systems. In: Dodge, D.P., Ed., Proceedings of the International Large River Symposium (LARS), Canadian Journal of Fisheries and Aquatic Sciences Special Publication 106, NRC research press, Ottawa, 110-127.

Lettenmaier, D. P., Alsdorf, D., Dozier, J., Huffman, G. J., Pan, M. & Wood, E. F. (2015). Inroads of remote sensing into hydrologic science during the WRR era. Water Resources Research, 51(9), 7309-7342.

Margono, B. A., Bwangoy, J. R. B., Potapov, P. V., & Hansen, M. C. (2014). Mapping wetlands in Indonesia using Landsat and PALSAR datasets and derived topographical indices. Geo-spatial Information Science, 17, 60–71.

McFEETERS, S. K. (1996). The use of the normalized difference water index (NDWI) in the delineation of open water features. International Journal of Remote Sensing, 17(7), 1425-1432.

Murray, N. J., Phinn S. R., DeWitt, M., Ferrari, R., Johnston, R., Lyons, M. B., Clinton, N., Thau, D., Fuller, R. A. (2019). The global distribution and trajectory of tidal flats. Nature 565: 222-225.

Ordoyne, C., & Friedl, M. A. (2008). Using MODIS data to characterize seasonal inundation patterns in the Florida everglades. Remote Sensing of Environment, 112(11), 4107-4119.

Overton, I. C. (2005). Modelling floodplain inundation on a regulated river: integrating GIS, remote sensing and hydrological models. River Research & Applications, 21(9), 991-1001.

Planet Team (2018). Planet Application Program Interface: In Space for Life on Earth. San Francisco, CA. https://api.planet.com.

Robertson, A. I., Bacon, P., & Heagney, G. (2001). The responses of floodplain primary production to flood frequency and timing. Journal of Applied Ecology, 38(1), 126-136.

S ánchez-Rodr guez, Antonio Rafael, Chadwick, D. R., Tatton, G. S. , Hill, P. W. , & Jones, D. L. . (2018). Comparative effects of prolonged freshwater and saline flooding on nitrogen cycling in an agricultural soil. Applied Soil Ecology, 125, 56–70.

Schumann, J. P., & Moller, D. K. (2015). Microwave remote sensing of flood inundation. Physics and Chemistry of the Earth, 83-84, 84-95.

Song, C., Ke, L., Pan, H., Zhan, S., Liu, K., & Ma, R. (2018). Long-term surface water changes and driving cause in Xiong'an, China: from dense Landsat time series images and synthetic analysis. Science Bulletin, 63, 708–716.

Syvitski, P. M. f., Overeem, I., Brakenridge, G. R., & Hannon, M. (2012). Floods, floodplains, delta plains — a satellite imaging approach. Sedimentary Geology, (267–268), 1–14.

Tulbure, M. G., Broich, M., Stehman, S. V., & Kommareddy, A. (2016). Surface water extent dynamics from three decades of seasonally continuous Landsat time series at subcontinental scale in a semi-arid region. Remote Sensing of Environment, 178, 142-157.

Tockner, K., Malard, F., & Ward, J. V. (2000). An extension of the flood pulse concept. Hydrological Processes, 14(16-17), 2861-2883.

Thomas, R. F., Kingsford, R. T., Lu, Y., & Hunter, S. J. (2011). Landsat mapping of annual inundation (1979–2006) of the Macquarie Marshes in semi-arid Australia. International Journal of Remote Sensing, 32(16), 4545-4569.

USDA Forest Service Remote Sensing Applications Center, and U.S. Geological Survey, 2015, National Land Cover Database (NLCD) Percent Tree Canopy Collection: U.S. Geological Survey.

U.S. Geological Survey (2008). Calculating Flow-Duration and Low-Flow Frequency Statistics at Streamflow-Gaging Stations. Scientific Investigations Report 2008–5126.

U.S. Geological Survey. National Elevation Dataset, 2013-01-01. https://data.tnris.org/.

Venables, W. N. & Ripley, B. D. (2002). Modern applied statistics with S. Fourth edition.

Ward, D. P., Petty, A., Setterfield, S. A., Douglas, M. M., Ferdinands, K., & Hamilton, S. K., et al. (2014). Floodplain inundation and vegetation dynamics in the alligator rivers region (Kakadu) of northern Australia assessed using optical and radar remote sensing. Remote Sensing of Environment, 147, 43-55.

Wong, J. X. W., Van Colen, C., & Airoldi, L. (2015). Nutrient levels modify saltmarsh responses to increased inundation in different soil types. Marine Environmental Research, 104, 37-46.

Wu, H., Adler, R. F., Tian, Y., Huffman, G. J., Li, H., & Wang, J. J. (2014). Real-time global flood estimation using satellite-based precipitation and a coupled land surface and routing model. Water Resources Research, 50(3), 2693-2717.

Xu, H. (2006). Modification of normalized difference water index (NDWI) to enhance open water features in remotely sensed imagery. International Journal of Remote Sensing, 27(14), 3025-3033.

Zhao, X., Stein, A., & Chen, X. L. (2011). Monitoring the dynamics of wetland inundation by random sets on multi-temporal images. Remote Sensing of Environment, 115(9), 2390-240.